The Mt. Fuji Submillimeter-Wave Telescope

Yutaro Sekimoto[1], Satoshi Yamamoto, Masafumi Ikeda, Hiroyuki Maezawa, Tetsuya Ito, Gaku Saito

Research Center for the Early Universe and Department of Physics, University of Tokyo, Tokyo 113-0033

Ken'ichi Tatematsu, Yuji Arikawa[2], Yoshiyuki Aso, Takashi Noguchi, Keisuke Miyazawa, Sheng-Cai Shi[3]

Nobeyama Radio Observatory, National Astronomy Observatory of Japan, Nagano 384-1305

Shuji Saito[4], Hiroyuki Ozeki[5], Hideo Fujiwara[6]

Institute for Molecular Science, Okazaki 444-8585

Junji Inatani

National Space Development Agency of Japan (NASDA), Tsukuba 305-8505

Masatoshi Ohishi

National Astronomy Observatory of Japan, Tokyo 181-8588

and

Kazufusa Noda, Yuichi Togashi

Oshima Prototype Engineering Co., Ltd., 3-10-28 Nishikubo, Musashino, Tokyo 180-0013

To appear in Review of Scientific Instruments July 2000

[1]Present address: Nobeyama Radio Observatory, National Astronomy Observatory of Japan

[2]also Department of Astronomical Science, The Graduate University for Advanced Studies

[3]Present address: Purple Mountain Observatory, 2 west beijing road, Nanjing, JiangSu 210008, China

[4]Present address: Fukui University, Fukui 910-8507

[5]Present address: National Space Development Agency of Japan (NASDA)

[6]Present address: Department of Chemical System Engineering, School of Engineering, University of Tokyo, Tokyo 113-8685

Abstract

We have developed a 1.2 m submillimeter-wave telescope at the summit of Mt. Fuji to survey emission lines of the neutral carbon atom (C_I) toward the Milky Way. A superconductor-insulator-superconductor (SIS) mixer receiver on the Nasmyth focus is used to observe the 492 GHz band in SSB and the 345 GHz band in DSB simultaneously. The receiver noise temperature is 300 K in SSB and 200 K in DSB for 492 and 345 GHz, respectively. The IF frequency is $1.8 - 2.5$ GHz. An acousto-optical spectrometer (AOS) which has the total bandwidth of 0.9 GHz and 1024 channel outputs has been also developed. The telescope was installed at the summit of Mt. Fuji (alt. 3725 m) in July 1998. It has been remotely operated via a satellite communication system from Tokyo or Nobeyama. Atmospheric opacity at Mt. Fuji was 0.4 - 1.0 at 492 GHz during 30 % of time and 0.07 - 0.5 at 345 GHz during 60 % of time from November 1998 to February 1999. The system noise temperature was $1000 - 3000$ K in SSB at 492 GHz and $500 - 2000$ K in DSB at 345 GHz. We observed the CI ($^3P_1 - ^3P_0$: 492 GHz) and CO ($J = 3 - 2$: 345 GHz) emission lines from nearby molecular clouds with the beam size of $2.'2$ and $3.'1$, respectively. We describe the telescope system and report the performance obtained in the 1998 winter.

1 Introduction

Distribution of interstellar gas in the Galaxy has been explored with the 21 cm line of the hydrogen atom (HI), the 2.6 and 1.3 mm lines of CO, and the 158 μm line of the ionized carbon atom (CII). Observations of the HI lines revealed the total distribution of diffuse atomic gas in the Galaxy, and the CII observations demonstrated wide existence of diffuse photon dominated regions. By contrast, the CO observations clarified the distribution of dense molecular gas, which is directly related to formation process of new stars. Although distributions of atomic gas and molecular gas have been unveiled through the above studies, the possible interchange process between these two ultimate phases has yet to be well understood. Observations of the neutral carbon atom (CI), which traces an intermediate stage between the atomic and molecular clouds, should be essential. When we consider formation of molecular clouds from diffuse atomic clouds, the major form of the gas phase carbon changes from CII to CI, and then from CI to CO (e.g.[1]). Carbon is the fourth most abundant element after hydrogen, helium, and oxygen in space, and its ionization potential of 11.266 eV is the lowest among the abundant atoms.

In diffuse clouds where the interstellar ultraviolet radiation penetrates, most molecules are dissociated and the carbon atom is photo-ionized. As a result, the major form of the gas phase carbon is CII. As the density of the cloud increases, the ultraviolet radiation, which can ionize the carbon atom, cannot penetrate to shielded in the inner part of the cloud. In this situation, the neutral carbon atom becomes abundant. As the density further increases, the carbon atom reacts with oxygen containing species (e.g. OH, O_2) to form a stable molecule, CO. Therefore we can study the formation process of molecular clouds by comparing the distributions of CII, CI, and CO.

CI has two submillimeter-wave magnetic dipole allowed transitions between the three fine structure levels of the ^3P ground electronic state. The transitions are $^3P_1 - ^3P_0$ and $^3P_2 - ^3P_1$ with frequencies 492.1607 GHz [2] and 809.3435 GHz [3], respectively. These lines were first detected by Phillips et al.[4] with Kuiper Airborne Observatory (KAO) and by Jaffe et al.[5] with the U-

niversity of Hawaii 2.2m telescope. The critical density of these lines is as low as 1000 cm^{-1} [6]. Therefore the CI line is expected to be observed widely over molecular clouds. In fact, the FIRAS on COBE with a 7° beam has revealed that large amount of CI exists on the Galactic plane[7][8].

However, apart from COBE, CI observations have so far been limited to small regions of representative objects. This is because most observations have been carried out with large submillimeter-wave telescopes such as the JCMT (dia. 15 m) and the CSO (dia. 10.4 m). Such telescopes are suitable for studying detailed structure with high spatial resolution of $\sim 10''$, but not to explore the large area distribution of CI in molecular clouds. Some projects for large-scale surveys of CI have recently been initiated; the AST/RO 1.7 m diameter telescope with the $1.'5$ beam at the south pole (alt 2835 m) [9]; the KOSMA 3 m telescope at Gornergrat (alt. 3150 m) [10][11]; the CSO focal reducer system with the $3'$ beam [12]; the Submillimeter Wave Astronomical Satellite. In spite of these efforts the observed area is still much smaller than that for the CO lines.

In fact, the distribution of CO in molecular clouds has been extensively studied by several small sized telescopes. Most significantly, the Columbia 1.2 m telescopes have surveyed in the CO ($J = 1 - 0$) line with an $8.'7$ beam toward the Milky way [13][14]. Very small telescopes with 60 cm diameter [15] at Nobeyama and Chile have made surveys in the CO ($J = 2 - 1$) line with the same beam size as the Columbia telescopes. The Nagoya 4 m [16] and NANTEN [17] telescopes also have conducted CO ($J = 1 - 0$) and ^{13}CO ($J = 1 - 0$) surveys of nearby molecular clouds with the moderate angular resolution of a $2.'7$ beam.

For our purpose in studying the formation process of molecular clouds, we need a small sized telescope with high sensitivity in order to map the whole of a molecular cloud within a reasonable time. On the basis of this motivation, we have developed the 1.2 m submillimeter-wave telescope system as described below.

2 Site

Mt. Fuji is a dormant volcano with 600 m diameter crater, and isolated from major mountains in the mainland of Japan. It is located at E 138° $43'$ $38''.3$, N 35° $21'$ $43''.9$, about 100 km west of Tokyo and about 100 km south of Nobeyama. In winter months, low-temperatures around $-20°C$ and fine days persist because the high-pressure system from Siberia covers Japan. The average wind speed at the summit is 10 and 15 m s^{-1} in summer and winter, respectively.

Sekimoto et al.[18] reported the atmospheric opacity at 220 GHz at the summit of Mt. Fuji (alt. 3776 m) for two years. The 220 GHz opacity was lower than 0.06 for a significant fraction ($\sim$ 45 %) of time from November 1994 to March 1995 [18]. Diurnal variation of the opacity at the summit of Mt. Fuji is so small that continuous observations at submillimeter-wave bands are possible through day and night.

The telescope site is *Nishi-yasugawara* (3725 m), which is 200 m north of the highest peak, *Kengamine* (3776 m). In summer, the telescope site is accessible by a bulldozer which can transport a maximum load of 1 ton. The electric power has been supplied in the 220 V line from the weather station of the Meteorological Agency at *Kengamine*.

3 Instrument

A schematic drawing and a photograph of the Mt. Fuji submillimeter-wave telescope is shown in Fig. 1 and Fig. 2, respectively. The parameters of the telescope are listed in Table I.

3.1 Antenna

3.1.1 Main reflector

A high precision 1.2 m main reflector with a focal length of 0.48 m has been developed (Fig. 3, 4). We used Al 5052 for the material because of its good machinability. To form the main reflector, an aluminum plate of 20 mm thick was pressed and curved. The curved aluminum plate was then welded to the backing structure. The stress in the plate has been released by a controlled heat treatment lasting two months. The plate was cut to a parabolic shape with 15 mm thickness by a lathe with 1.2 m diameter.

The surface accuracy was measured with a parabolic template and a feeler gauge of 10 μm. The parabolic template has an accuracy of 8 μm peak-to-peak, which was measured by a three-dimensional position sensor as shown in Fig. 5. The main reflector was hand polished by comparing with the template. Then we confirmed that there is no space for the feeler gauge of 10 μm between the main reflector and the template on all areas of the main reflector. There is no surface coating for the main reflector.

The backing structure of the main reflector has a square pattern with a rib of height 150 mm, width 15 mm, and pitch 300 mm, which reduces the gravitational deformation (see Fig. 6). There are many holes with about 50 mm diameter in the backing structure and antenna structure to reduce the weight and to circulate the air. The total weight of the main reflector is 81 kg.

3.1.2 Antenna structure

Almost all mechanical components above the azimuth motor were selected to have the same thermal expansion coefficient as Al 5052, thus the antenna will deform homologously with temperature. As an exception, stainless steel has to be used exceptionally for the elevation motor and its bearing system. In such cases, we designed an offset mechanism to avoid the thermal stress caused due to difference in thermal expansion between stainless steel and aluminum.

A rigid box at the intersection between the azimuth and elevation axes connects the main reflector, the elevation drive motor, the elevation bearing, the and counter balance (see Fig. 4). The size of the elevation box is $30 \times 30 \times 30$ cm^3 and 22 kg in weight. The counter balance attached on the elevation axis is made of lead with 110 kg weight.

The antenna structure is mounted on a control cabin, $2 \times 2 \times 2$ m^3. The azimuth table was aligned to horizontal level within $2'$ at the legs of the control cabin when the telescope was installed. Three standard racks containing instruments are mounted in the cabin (see Fig. 1).

3.1.3 Drive system

Direct drive motors are used to control the azimuth (NSK M-RS1410) and elevation axes (NSK M-RS1010). The components of these motors were modified to have a similar thermal expansion

to the steel. The torque of motors is 235 and 147 N m for azimuth and elevation axes, respectively. The inertia around the azimuth and elevation axes is $\sim$ 100 and 27 kg m^2, respectively. The maximum velocity and maximum acceleration of the motors are limited to 3.6 $^\circ$s^{-1} and 3.6 $^\circ$s^{-2}, respectively, to minimize overshooting. On the both axes, we employ an optical encoder (Heidenhain RON 255) with an absolute accuracy of 1$''$ and a magnetic resolver with 2$''$ resolution and 30$''$ accuracy. All grease used for this telescope is good for temperatures below -30°C. Four limit switches are equipped for both directions of azimuth ($\pm 190^\circ$) and elevation axes ($20^\circ - 100^\circ$). An electromagnetic brake is also installed for the both axis.

3.1.4 Sub-reflector

The hyperbolic subreflector with 72 mm diameter is supported by four feed-legs. The subreflector hides a stepping motor and a ballscrew to adjust the focal length with range of $\pm$ 0.5 mm and resolution of 10 μm. The subreflector and main reflector have an edge taper of -20 dB to optimize not aperture efficiency but main beam efficiency of the survey telescope (cf. [19]). The cross section of a feed-leg is a triangle pointed to the main reflector.

3.2 Optics

We designed the frequency independent optics between the subreflector and feed horns based on a Gaussian beam propagation [19], [20],[21] (see Fig. 4, 6, 7). To achieve high beam efficiency, the optics from the hyperboloidal subreflector (Dia. 72 mm) to the mixer horns located at the Nasmyth focus involve minimum optical components: 2 ellipsoidal mirrors, 1 plane mirror and 3 wire grids (Fig. 4). The optical components except for the subreflector were designed for a Gaussian beam with an edge-level of less than -30 dB at 340 GHz. Thus, RF signals between 340 and 900 GHz are observable because of the frequency independent optics. To reduce an asymmetry of the beam generated at ellipsoidal mirrors, reflection angles at ellipsoidal mirrors were designed to as small as 22.5 degree.

The surface of the main reflector is described as

$$z = \frac{x^2 + y^2}{4f} + z_e, \tag{1}$$

where the origins of the coordinate are the elevation and azimuth axes. In the elevation box at the intersection of the azimuth and elevation axes, an elliptical mirror 1 (EM1) and a plane mirror (PM) are mounted. The distance between the elevation axes and the apex of the main reflector ($z_e = 270$ mm) is designed to be short as possible to minimize the size of mirrors in the elevation box. The short distance also reduces the counter weight. Two hot loads for temperature calibration are also located in the elevation box. One of the hot loads is planned to be warmed to 60 $^\circ$C by a heater for more accurate intensity calibration.

For frequency independence, we determined parameters using the following relations under the assumption of Gaussian optics [20];

$$\frac{\omega_s}{\omega_i} = \frac{L_s}{L_{i1}}, \tag{2}$$

$$\frac{1}{f_1} = \frac{1}{L_{i1}} + \frac{1}{L_s}, \tag{3}$$

$$L_{i1}(1+\frac{L_{i1}}{R_i}) = -L_s(1-\frac{L_s}{R_s}), \tag{4}$$

$$\frac{\omega_h}{\omega_i} = \frac{L_2}{L_{i2}}, \tag{5}$$

$$\frac{1}{f_2} = \frac{1}{L_{i2}} + \frac{1}{L_2}, \tag{6}$$

and

$$L_2(1+\frac{L_2}{R_h}) = -L_{i2}(1-\frac{L_{i2}}{R_i}). \tag{7}$$

The definition of the parameters is given in Fig. 7. The optics and the mechanical structure of the telescope were iteratively optimized. Parameters for the telescope are tabulated in Table II, and the calculated beam diameter at 345, 492, and 809 GHz is shown in Fig. 8.

3.3 Frontend

3.3.1 Receiver

We developed an SIS (Superconductor-Insulator-Superconductor) receiver which can receive both the 492 (CI) and 345 GHz (CO $J = 3 - 2$) bands simultaneously by observing orthogonal polarizations (see Fig. 9,10). We employed a Nb-based parallel connected twin junction (PCTJ)[22] for the 345 GHz mixer and a Nb-based distributed 10 junction (DJ10) for the 492 GHz mixer.

The 492 GHz signal is received in lower side-band (LSB) with a new quasi-optical SSB mixing method [23]. Its principle has been realized for 100 GHz bands by Phillps and Jefferts[24], however, our method is new in that RF and LO signals are divided and coupled by means of a single wire grid. The RF signal is fed to two mixer horns with a phase difference of 180 degree, but the LO signal is with that of 270 degree. The latter phase difference is generated by a reflective circular polarizer composed of a plane mirror and a wire grid with 110 μm separation. After the IF signals are diplexed with 90 degree phase difference, the USB and LSB signals are obtained (Fig. 10). We used only the LSB signal.

The Y factors of two SIS mixers were independently measured in DSB at various I-V points in the laboratory. The LO power for two mixers is adjusted simultaneously. On the other hand, mixer bias for two mixers is applied independently. Each mixer had a noise temperature of 120 K in DSB. By combining the two mixers, the receiver had a noise temperature of 300 K in SSB at 492 GHz. We measured the image rejection ratio by using higher-order frequency emission from the 345 GHz LO. The ratio was roughly 0.9 in the IF band between 1.8 and 2.5 GHz.

The 345 GHz signals are received as upper side-band with a mixer operation in DSB mode. The receiver noise temperature was 200 K in DSB at 345 GHz. The estimated loss of the RF signal due to various components, from the radome to the mixer horn, is summarized in Table III.

RF signal enters the dewar and is split into the 345 and 492 GHz signals by a cooled wire grid 1 (WG1). The 345 GHz signal is reflected by WG2, then, is reflected at an ellipsoidal mirror (EM2) to the mixer horn. The 492 GHz signal is split into two signals by WG3, and then the signals are reflected at EM2 to the mixer horns. The distance between WG3 and EM2 is 100 mm. There is a polarization grid (WG4) at the front of the mixer horn to reject cross-polarization components generated by the mixer horn. All these optical components in the dewar are cooled to about 5 K. The unwanted signals are terminated by an absorber at a temperature around 5 K.

3.3.2 Mixer block

The mixer block and its diagonal horn were integrally formed by electroforming. The horn feeds the RF and LO signals to the mixer-chip via the half-height waveguide with a fixed backshort cavity. The size of the waveguide is 508 μm in width $\times$ 127 μm in height for 492 GHz and 736 μm in width $\times$ 184 μm in height for 345 GHz. For the 492 GHz band, two horns and two mixers are integrated in a mixer block (see Fig. 10). The Josephson current of the SIS mixer is suppressed by applying a magnetic field of $500 - 800$ gauss. The field is generated by 2 permanent magnets.

A bias circuit for the SIS mixer is shown in Fig. 12. The circuit is inserted in the mixer bock for the 345 GHz, but is mounted in a box with the 90 degree hybrid for the 492 GHz band. By optimizing a choke inductor and a capacitor for a noise filter, the return loss for the IF signal is less than -25 dB at room temperature. The dc bias for 3 SIS mixers is independently applied by a bias driver (Nittuki 8842 G), which is controlled via GPIB.

3.3.3 Local oscillator

The LO signals for 492 and 345 GHz are generated by multiplying the output of a W-band ($\sim$ 80 GHz) Gunn diode oscillator with 3×2 and 2×2 multipliers (Radiometer Physics GmbH.), respectively. The LO power ($\sim$ 1 mW) is mainly adjusted by a mechanical attenuator. For the 492 GHz, we also adjusted the power by controlling the bias voltage of the multiplier. The LO frequency is stabilized to a synthesized signal generator in the 4 GHz region by the phase-locked loop (PLL) as shown in Fig. 12. The PLL is adjusted and locked by remote control. The Doppler tracking is carried out by adjusting the frequency of the signal generator.

The LO signals are quasi-optically coupled to the RF signals by cooled free-standing grids in the dewar (see Fig. 10). The polarization and LO coupling grids have Invar frames and tungsten wires with 20 μm diameter and 60 μm pitch (Thomas Keating Co.). The LO coupling ratio to the RF signal is 5 % at 492 GHz and 3 % at 345 GHz. The LO power of the both frequencies is sufficient, so that the ratio will be reduced in the future.

3.3.4 Cryogenics

The receiver employs a 2-stage Gifford-MacMahon cryocooler, which has a cooling capacity of 0.3 W on the 4 K cold stage and 1 W on the 40 K stage with 3 kW power consumption (Sumitomo RD 203 L4). The receiver dewar and the cooled optics is made of Al so that the weight of dewar including the refrigerator (18 kg) is 40 kg. The compressor for this cryocooler is cooled by water circulation. A vacuum pump, composed of a rotary pump and a turbo-molecular pump, evacuates the receiver dewar to the order of 10^{-4} mbar before cooling. The compressor, the water circulator, and the vacuum pump are mounted on the azimuth table.

The operating temperatures of the 4 K stage and the 40 K stage were 5 K and 50 K, respectively. It takes 7 hours to cool the receiver from room temperature to the operating temperature. Though the temperature variation of the cryocooler is 0.2 K at the head of the 4 K stage, it is reduced to 0.02 K at the mixer because the 400 g aluminum block for the 4 K optics serves as a thermal buffer.

An RF window of 32 mm diameter on the vacuum dewar employs a Kapton sheet of 12.5 μm thickness. The loss of the RF signal due to the Kapton is calculated to be 2 and 1 % at 492 and

345 GHz, respectively. Two LO windows of 26 mm diameter are Mylar sheets of 100 μm thickness. A radiation shield on the 40 K stage is a fibrous-porous form of PTFE (Zitex G106) with 150 μm thickness and a pore of 50 %. The semi-rigid cables for IF signals are made of CuNi. We use a cable made of phosphor-bronze for the mixer bias. Thermal inputs to the dewar are estimated in Table IV. To reduce thermal radiation from the 300 K wall to the 40 K shield, a multi-layer thermal insulator is attached inside the 300 K wall.

3.3.5 Alignment of the receiver

To align the optical axes of the telescope and the receiver optics we employed a simple method using a diode laser. Two pin-holes with 1 mm diameter separated by 50 mm are put at the position of the mixer horn with an accuracy of 10 μm and they are used to define the optical axis of the receiver optics. The laser beam passing through these two holes illuminates the sub-reflector with a spot size of 2 mm diameter. We adjusted the position of the receiver at the room temperature using a three-dimensional mechanical stage between the receiver and the azimuth table so that the laser beam coincided with the center of the subreflector within 1 mm at a distance of 1.5 m, even if the elevation angle of the main reflector changes from 90 degree to 20 degree. We included that 1 mm contraction of the cryocooler at the operating temperature. This method aligns the receiver with respect to the antenna optics with an angular accuracy of $3'$.

3.4 Backend

3.4.1 IF

The IF diagram is shown in Fig. 13. The intermediate frequency is $1.8 - 2.5$ GHz. The IF signals from the mixers are independently amplified by two cooled low noise amplifiers (LNA, Nitsuki 9838S4) attached to the 40 K stage. The LNA is composed of 3 GaAs FETs, each with a power consumption of 5 mW. An isolator is placed between the mixer block and the LNA.

After amplification by 40 dB at room temperature, the 492 and 345 GHz signals are fed to an IF selector. In order to avoid electromagnetic interference from the weather station's radar, which is operated with the frequency of 2.88 GHz, dedicated filters have been used in the main IF line, whose suppression level is -60dB at the radar frequency. Then, it is lead to the acousto-optical spectrometer (AOS) in the control cabin. The outputs of the noise diode and comb generator are also coupled to the main IF line. These are used to check AOS performance and to calibrate the frequency axis. At the input of the AOS, the -20 dB IF signal is fed to a detector to monitor the total power. The length of the cables from the antenna to the control room, including the wrapping length at the azimuth axis is 5 m.

3.4.2 AOS

A wide band AOS has been developed for the backend [25]. The spectrometer was designed by reference to that built in the university of Cologne [26],[27]. A bragg cell made by GEC Marconi (Y-36-1446-02) was used. Prior to mounting it to the spectrometer system, the cell was held at -30 °C and $+50$ °C for several hours to check that no degradation was observed in its performance. The laser diode (Hitachi HL-7851G) was temperature controlled at 25 ± 0.1 °C by a peltier device.

The imaging optics enables us to cover 900 MHz bandwidth with a 1024 channel CCD array. The effective frequency resolution is set to 1.6 MHz. The frame rate was set to 10 ms and the readout data of the CCD is accumulated by a simple adder. The integrated data are sent to a host machine through GP-IB interface. The spectroscopic Allan variance minimum time was found to be more than 60 s. Thanks to compensation of the frequency characteristics between the IF system and AOS, the gain variation of the spectrum observed at the AOS is less than 2 dBp-p over 700 MHz band width as depicted in Fig. 14. The spectrometer unit was surrounded by a resinous material with thickness of 3 cm so that thermal isolation is partially achieved.

3.5 Radome

To protect the antenna from wind and precipitation, we employ a 2.9 m diameter radome made by ESSCO. From an experiment using a small radome at the summit of Mt. Fuji in 1994 and 1995 [18], we expected that the radome surface supplied with an adequate thermal flux is free from accumulation of ice and snows on the radome.

The radome consists of 40 triangle panels made of Al 6061 frames (see Fig. 3, 6), whose average blockage for the RF signal is 11 %. The radome has no protuberance such as screw caps on outside surface not to coat ice and snow. The weight of the radome is 160 kg. The inside diameter of the radome is 2.67m. The membrane is made of 0.3 mm thick woven-Teflon (Gore-Tex) which has transparency of 81 % and 89 % at 492 and 345 GHz, respectively. The radome with 10 segments at the base is supported by a radome tower (see Fig. 1). The radome tower stands directly from the foundation, so that it is independent from the antenna structure/control cabin. This design reduces the effects of vibrations due to strong winds and the effects of thermal expansion of the tower due to solar radiation. The height of the radome tower of 2.9 m was determined from the average snow depth of 2.0 m at the summit of Mt. Fuji in winter.

Two blower fans with 0.5 kW each power consumption circulate the air between the radome and the cabin so as to keep uniform temperature.

3.6 Optical camera

A light weight CCD camera with lens (750 g) is mounted at the upper edge of the main reflector for the purpose of the optical pointing. The lens (Tamuron SP500F/8) composed of two reflective mirrors has a focal length of 500 mm in spite of compactness ($\phi 84 \times 91.5$ mm, 535 g). A pixel of the CCD corresponds to $3'' \times 3''$. The integration time of the CCD is set to 100 ms by two external triggers. The system can detect a 5 magnitude star above 10 σ with 0.1 s integration. The five radome panels at the top were removed to carry out the optical pointing with the CCD camera.

3.7 Control System

We have developed a remote control system for the telescope by using a commercial satellite communication system (JC satellite). All instruments are controlled by a MicroSPARC-II-based CPU board (Force SPARC CPU-5V) with VME bus via GP-IB and RS-232C interfaces. The operating system is Sun OS 4.1. The standard time is adjusted by NTP (network time protocol) system operated by National Astronomical Observatory of Japan and by GPS (global positioning system).

3.7.1 Communication

We used satellite communication at a speed of 64 kbps in the 14/12 GHz band for the telescope control, monitoring, and data transfer. The geostationary satellite is JCSAT-1. We employed two antennas: one with 60 cm width and 82 cm height in the annex of the telescope (see Fig. 1) and the other with 1.2 m width is installed in Nobeyama Radio Observatory. The window material for the latter antenna is Teflon with 1 cm thickness. This system was very reliable during observations.

For the backup purpose, we used a serial communication method via a satellite mobile phone (NTT N-star system) at a speed of 2400 bps. This system uses the S-band (2.6/2.5 GHz). A small antenna (20×20 cm^2) was mounted at the inside edge of the radome.

3.7.2 Software

We have developed observation control software including a quick-look capability. The software is run on the CPU at the summit and the telescope status and various instrumental parameters and house-keeping parameters are monitored by using X-window protocols via TCP/IP from Tokyo and Nobeyama. The telescope control software has a simple, multi-tasking structure, which was designed to have high reliability. We employed the character-based user-interface for control commands and the monitor of telescope status. This reduces the communication load under the limited speed of the satellite communication. We prepare various mapping methods with position switching. A frequency switch is also supported.

The data are stored in the FITS format on the hard disk. We analyze the data using the Newstar package developed by Nobeyama Radio Observatory.

3.7.3 Monitor system

The monitor system for receiver tuning and house-keeping uses a PGPLOT package developed by California Institute of Technology. The phase lock spectrum from a spectrum analyzer, the AOS band characteristic from a oscilloscope and variation of the total power are monitored. House-keeping data such as temperature and relay status are also monitored every minute. The overhead of mapping observations including the frequency and intensity calibrations and the antenna movement was 40 % of the accumulation time.

In the case of an electricity failure, some instruments are safely halted by the CPU backuped with uninterrupted power supply (UPS) and others are automatically stopped without judgment by the CPU. For example, the vacuum valve of the receiver is closed automatically and the refrigerator is shut down by CPU on power failure in order that they do not start automatically at the recovery.

4 Atmospheric condition

The atmospheric conditions at the summit of Mt. Fuji are very good for submillimeter-wave observations in winter. We measured the atmospheric opacity occasionally by tipping the main reflector. An example of the opacity measurements at 492 GHz is shown in Fig. 15. Fig. 16 shows the distribution of opacity at 492 and 345 GHz, atmospheric temperature and dew point for ten days from February 10, 1999. The atmospheric temperature and dew point were measured by the weather station at the summit. The opacity and dew point are roughly correlated.

The zenith opacity of 492 GHz was from 0.4 to 1.0 over ~30 % of time in winter 4 months from November to February. These results are consistent with the 220 GHz opacity measurements at the summit of Mt. Fuji [18] and a model calculation at 4800 m in Chile [29], [30]. We note that the opacity at 492 GHz during the Austral winter and spring at the south pole (alt. 2835 m) was below 1.0 over 85 % of the time [31]. The zenith opacity of 345 GHz ranged from 0.07 to 0.5 over ~ 70 % of time in winter months.

5 Performance

5.1 Optical pointing

The pointing calibration was carried out by measuring the apparent position of 100 stars with a CCD camera on September 1998. We utilized a software, STARLINK library developed by the Rutherford Appleton Laboratory, to calculate the Az-El position from the right ascension and declination. The instrumental errors are removed by fitting seven parameters in following equations [32];

$$\begin{aligned} dAz &= -x_1 \times \cos(x_2 - Az) \times \tan(El) \\ &\quad +x_3 \times \tan(El) + x_4/\cos(El) + x_5, \end{aligned} \tag{8}$$

and

$$dEl = -x_1 \times \sin(x_2 - Az) + x_6 \times El + x_7. \tag{9}$$

The fitted parameter is tabulated in Table V.

5.2 Radio pointing

The radio pointing was carried out by observing the Sun and the Moon in the 345 GHz continuum at least once in a month (Fig. 17). The instrumental errors for the radio pointing are also removed with the method used in the optical pointing (Table V). During the winter months, we maintained the pointing accuracy with 20″ rms. We confirmed that the 345 and 492 GHz beams coincide with each other within 20″. We made 9 point observations of Orion KL and M17 with a 1.′5 grid every day to confirm the pointing accuracy as well as the intensity scale.

5.3 Moon efficiency

The moon efficiency including the radome loss (η_{mR}) was measured by observing the Moon at the full (see Fig. 17). The moon efficiencies at 492 GHz and 345 GHz were derived to be 0.72 and 0.75, respectively, by assuming the brightness temperature of the full Moon to be 355 K [33]. Since the radome loss is calculated to be 90 %, we derive the moon efficiency of the telescope (η_{moon}) at 492 and 345 GHz to be 0.80 and 0.83, respectively.

5.4 Intensity calibration

Antenna temperature (T_a) was derived by the standard chopper-wheel method every 3 minutes. Then, it were converted to the radiation temperatures T_R^* [34] by correcting for the moon efficiency

including the radome loss (η_{mR}) and for a difference between sky and radome temperatures (η_{corr}).

$$T_R^* = T_A \times \eta_{corr}/\eta_{mR}/\eta_{irr}. \tag{10}$$

The correction factor (η_{corr}) was $1.05 - 1.2$ at 345 GHz and $1.2 - 1.4$ at 492 GHz depending on the atmospheric condition. We assumed that both sidebands at 345 GHz have an equal gain ($\eta_{irr} = 0.5$). An image rejection ratio is assumed to be -10 dB ($\eta_{irr} = 0.9$) for 492 GHz based on the measurements in the laboratory.

Intensities of the CI and CO ($J = 3 - 2$) lines toward Orion KL and M17 were monitored every day as far as they were observable. Fig. 18 shows $1.'5$ grid spectra at 492 GHz towards M17SW (RA (1950) = $18^h17^m30^s$, Dec (1950) = $-16°13'0''$). The ON and OFF time for each spectrum is 20 seconds and it takes 8 minutes to obtain nine spectra. The intensities at 492 GHz are consistent with that observed with a $3'$ beam by the KAO [35]. Though daily variations of the intensity were as large as ± 15 %, we normalized the main beam temperature based on the intensity calibration.

The half power beam widths at 492 and 345 GHz were measured to be $2.'2 \pm 0.'2$ and $3.'1 \pm 0.'2$, respectively, by scanning the Sun (See Fig. 17).

5.5 Spectra

We show a spectrum at 492 GHz toward Orion KL in Fig. 19. Some molecular lines (SO_2, H_2CO, CH_3OH and $(CH_3)_2O$) were detected as well as CI. Fig. 20 shows spectrum at 345 GHz towards Orion KL, which was obtained in the poor atmospheric condition. According to a line survey of Orion KL with CSO [36], the line around 345.34 GHz is $H^{13}CN$ (345.3398 GHz) or SO_2 (345.3385 GHz).

There remain interference fringes due to the IF cables in the spectra, which actually limit the sensitivity of the telescope system. It will be improved in the future.

6 Operational status

The telescope was pre-installed in the site of the Nobeyama Radio Observatory in June 1997. After we made test observations at 345 GHz from December 1997 to March 1998, it was disassembled for the transportation to the Mt. Fuji in June 1998. On 1998 July 29, the telescope was installed by a helicopter to the summit of Mt. Fuji. Since the beginning of November 1998, it has been continuously operated from University of Tokyo/the Nobeyama Radio Observatory via satellite communication system.

We have carried out large-scale mapping observations over 20 square degree of molecular clouds, HCL2 in TMC1 [37], Orion A [38], M17, NGC2264, W3, DR21, L134N, W44, W51, W28, ρ-Ophiuchuis, NGC1333 and MBM12 in the CI and CO ($J = 3 - 2$) lines from November 1998 to March 1999. The SSB system noise temperature at 492 GHz was $1000 - 3000$ K during the observations. The DSB system noise temperature at 345 GHz was $500 - 2000$ K. For example, Fig. 21 shows the distribution of the CI emission toward a giant molecular cloud, M17. Fig. 22 shows that of CO ($J = 3 - 2$) in the same region. These maps demonstrate a capability of the Mt. Fuji submillimeter-wave telescope to survey submillimeter-wave emission lines of the neutral carbon atom and the CO molecule.

We thank the staff of the weather station at the summit for their kind support to this project. We also thank the Meteorological Agency of Japan for the support to this project. We are grateful to Norio Kaifu and Hiroo Inokuchi for their encouragements. We thank Tomoharu Oka, Mitsuhiro Iwata, Tsuyoshi Sakai, Kazuhisa Kamegai, Hideta Habara, Ji Yang, Hiroshige Yoshida, Tomoya Hirota, Naritomo Shiki, Hiroshi Minowa, Eun Sok Kim, Hirokazu Seki, Yasuaki Hikita, Rintaro Fujimoto, Shigehisa Takakuwa, Kei Takayama for their cooperation. The authors are grateful to Norio Ikura and Shuichi Norizuki for their work of the telescope. The authors are indebted to R. Schieder for his valuable comments and to T. Horigome and H. Yoshida for their cooperation in constructing AOS. The Mt. Fuji submillimeter-wave telescope is developed as one of research projects of the Research Center for the Early Universe under the financial support by Grant-in-Aid from the Ministry of Education, Science, and Culture (No. 07CE2002). We thank the staff of Nobeyama Radio Observatory for their help to the pre-installation in the site. This study is partially funded by the joint research program of the Graduate University for Advanced Studies and by a part of "Ground Research for Space Utilization" promoted by NASDA and Japan Space Forum.

References

[1] H. Suzuki, S. Yamamoto, M. Ohishi, N. Kaifu, S. Ishikawa, Y. Hirahara, and S. Takano 1992, ApJ, 392, 551

[2] S. Yamamoto and S. Saito 1991 ApJ, 361, 318

[3] A. L. Cooksy, R. J. Saykally, J.M. Brown, M. K. Evenson 1986 ApJ 309, 828

[4] T. G. Phillips, P. J. Huggins, T. B. Kuiper, and R. E. Miller 1980, ApJ,238, L103

[5] D. T. Jaffe, A. I. Harris, M. Silber, R. Genzel, and A. L. Betz 1985, ApJ, 290, L59

[6] K. Schroder, V. Staemmler, M. D. Smith, D. R. Flower, & R. Jacquet 1991, J. Phys. B. 24, 2487

[7] E. L. Write et al. 1991 ApJ. 381, 200

[8] C. L. Bennet et al. 1994, ApJ. 434, 587

[9] A. A. Stark., R. A. Chamberlin, J. G. Ingalls, J. Cheng, G. Write 1997 Review of Sci. Instrum. 68, 2200

[10] Winnewisser, G. et al. 1986 AA 167, 207

[11] G. Winnewisser, P. Zimmermann, J. Hernichel, M. Miller, R. Schieder, and H. Ungerechts 1990, AA 230, 248

[12] R. Plume, & D. T. Jaffe 1995 PASP 107, 488

[13] R. S. Cohen, T. M. Dame, and P. Thaddeus 1986 ApJS, 60, 695

[14] L. Bronfman, H. Alvarez, R. S. Cohen, and P. Thaddeus 1989, ApJS, 71, 481

[15] S. Sakamoto, T. Hasegawa, M. Hayashi, T. Handa, T. Oka 1995, ApJS 100, 125

[16] K. Kawabata, H. Ogawa, Y. Fukui, T. Takano, Y. Fujimoto, R. Kawabe, K. Sugitani, & H. Takaba 1985 AA 151, 1

[17] Y. Fukui et al. 1999 Publ. Astron. Soc. Japan 51, 745

[18] Y. Sekimoto, H. Yoshida, T. Hirota, Y. Takano, E. Furuyama, S. Yamamoto, S. Saito, H. Ozeki, J. Inatani, M. Ohishi, A. G. Cariasmenos, and S. L. Hensel 1996, International Journal of Infrared and Millimeter Waves, **17**, No.7, 1263

[19] P. F. Goldsmith, 1998 IEEE Press "Quasioptical systems"

[20] T. S. Chu 1983 IEEE Trans. Antennas Propagation AP-31, 614

[21] P. F. Goldsmith, 1982, in Infrared and Millimter Waves, edited by K. J. Button (Academic press, New York) 277

[22] S. C. Shi, T. Noguchi, and J. Inatani 1997 IEEE Trans. Applied Superconductivity, 7, 2587

[23] J. Inatani, S. C. Shi, Y. Sekimoto, H. Mashiko, and S. Ochiai 1998, Ninth international symposium on space terahertz technology, 337

[24] T. G. Phillips and K. B. Jefferts 1973 Rev. Sci. Instrum. 44, 1009

[25] H. Ozeki, H. Fujiwara, H. Yoshida, T. Horigome, and S. Saito 1995 Ann. Rev. of Inst. Mol. Sci. II-B-2

[26] R. Schieder, V. Tolls, and G. Winnewisser, 1989 Exp. Astronomy 1, 101.

[27] M. Klumb, J. Frerick, V. Tolls, R. Schieder and G. Winnewisser 1994, SPIE 2268, 305.

[28] J. R. Birch, E. A. Nicol, and R. L. T. Street 1983, Applied Optics, 22, 2947

[29] T. Hirota, S. Yamamoto, Y. Sekimoto, K. Kotaro, N. Nakai, R. Kawabe 1998 PASJ 50, 155

[30] S. Matsushita, H. Matsuo, J. R. Pardo, and S. J. E. Radford 1999 PASJ 51, 603

[31] R. A. Chamberlin, A. P. Lane, and A. A. Stark, 1997 ApJ 476, 428

[32] M. L. Meeks, J. A. Ball and A. B. Hull 1968, IEEE, Ap-16,746, 1868

[33] J. G. Mangun 1993 AJ 105, 117

[34] M. L. Kutner, and B. L. Ulich 1981, ApJ 250, 341

[35] J. Keene, G. A. Blake, T. G. Phillips, P. J. Huggins, and C. A. Beichman, 1985 ApJ 299, 967

[36] P. Schilke, T. D. Groesbeck, G. A. Blake, and T. G. Phillips 1997 ApJS 108, 301

[37] H. Maezawa, M. Ikeda, T. Ito, G. Saito, Y. Sekimoto, S. Yamamoto, K. Tatematsu, Y. Arikawa, Y. Aso, T. Noguchi, S. C. Shi, K. Miyazawa, S. Saito, H. Ozeki, H. Fujiwara, M. Ohishi, and J. Inatani 1999, ApJ 524, L129

[38] M. Ikeda, H. Maezawa, T. Ito, G. Saito, Y. Sekimoto, S. Yamamoto, K. Tatematsu, Y. Arikawa, Y. Aso, T. Noguchi, S. C. Shi, K. Miyazawa, S. Saito, H. Ozeki, H. Fujiwara, M. Ohishi, and J. Inatani 1999, ApJ 527, L59

TABLE I. The Mt. Fuji submillimeter-wave telescope

parameter	
Parabolic main reflector:	
diameter	D = 1.2 m
focal length	f = 0.48 m
focal ratio	f/D = 0.4
weight	81 kg
surface accuracy	10 μm rms
material	Al 5052
Hyperbolic subreflector	D = 72 mm
Optics :	
elliptic mirror	2
plane mirror	1
cooled wire grid	3 (20μ tungsten wire)
Radome :	
diameter	2.92 m
membrane	Gore-Tex 0.3 mm thickness
frame	40 pieces made of Al 6061
Beam width (HPBW):	$2.'2$ @ 492 GHz
	$3.'1$ @ 345 GHz
Optical pointing:	$12''$ rms
Radio pointing:	$20''$ rms
Receivers:	SIS 492 & 345 GHz
Receiver noise temperature	300 K in SSB @ 492 GHz
	200 K in DSB @ 345 GHz
IF frequency	1.8 – 2.5 GHz
Backend :	AOS
AOS bandwidth	1.7 – 2.6 GHz
separation	0.9 MHz / channel
effective resolution	1.6 MHz
Moon efficiency	72 % @ 492 GHz
(including radome loss)	75 % @ 345 GHz
System noise temperature	> 1000 K in SSB @ 492 GHz
	> 500 K in DSB @ 345 GHz
Altitude	3725 m

TABLE II. Parameters of optics

parameter		[mm]
diameter of main reflector (MR)	D_m	1200
diameter of subreflector (SR)	D_s	72
focal lenth of main reflector	f	480
length between the apex of MR and the elevation axes	z_e	270
curvature of SR to the focus of MR	R_{s1}	28.07
curvature of SR to the horn	R_{s2}	430
Gaussian beam radius of SR	ω_s	24
distance between SR and elliptical mirror 1 (EM1)	L_s, z_1	891.0
distance between SR and elliptical mirror 2 (EM2)	z_2	1470.0
distance between SR and a horn	z_h	1515
distance between SR and plane mirror (PM)	z_p	792
distance between EM1 and intermediate image	L_{i1}	321
Gaussian beam radius of intermediate image	ω_i	8.6465
curvature of intermediate image to the horn	R_i	162.465
distance between the elevation axis and PM		70
distance between the azimuth axis and EM1		70
distance between EM2 and a horn	L_2	45
focal length of EM1	f_1	235.98
focal length of EM2	f_2	38.32
Gaussian beam radius of a horn	w_h	1.51
curvature of a horn	R_h	18.98
curvature of EM1 toward SR	R_{em1s}	477.90
curvature of EM1 toward horn	R_{em1h}	466.18
curvature of EM2 toward SR	R_{em2s}	148.55
curvature of EM2 toward horn	R_{em2h}	51.64

TABLE III. An estimated loss of the RF signal and the contribution to the noise temperature

	loss at 492 GHz	loss at 345 GHz	temperature at the loss	noise to 492GHz	noise to 345 GHz
	dB	dB	K	K	K
Radome frame	0.5	0.5	300	37	37
Radome membrane	0.9	0.5	300	70	37
main reflector	1.0	1.0	150	40	40
mirrors	0.2	0.2	200	10	10
dewar window	0.1	0.05	300	7	3
radiation shield	0.2	0.3	50	2	3
LO coupling	0.2	0.1	4	0.2	0.1
horn	0.5	0.5	4	0.5	0.5
Total	3.6	3.15	-	166.7	130.6

TABLE IV. Thermal input to the receiver

	4K stage	40 K stage
	[mW]	[mW]
Radiation from 300 K	10	(9000)[a]
Radiation from 50 K	50	470
IF cables	30	36
Bias cables	30	5
Amp power consumption	10	25
Sensor cables	30	8
Total	160	544

[a] The thermal input of radiation from 300 K is included in the specification of the cryocooler.

TABLE V. The fitted pointing parameters in the unit of degree

	optical	345 GHz
x_1	0.0164(2)	0.0911(5)
x_2	85.4113(6912)	118.2382(3037)
x_3	-0.0097(fix)	-0.0097(fix)
x_4	0.3715(4)	0.0582(17)
x_5	6.9767(1)	6.9422(24)
x_6	-0.0002(1)	0.0001(1)
x_7	0.1759(11)	0.2406(17)
data points	186	310
$1\ \sigma$	$11''$	$14''$

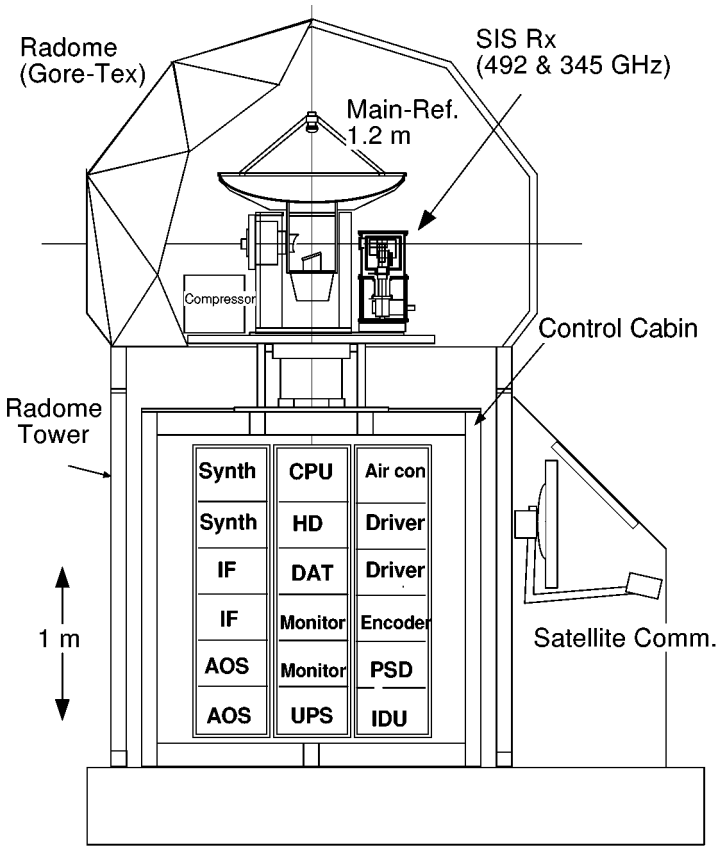

Figure 1: Schematic drawing of the Mt. Fuji Submillimeter-wave telescope.

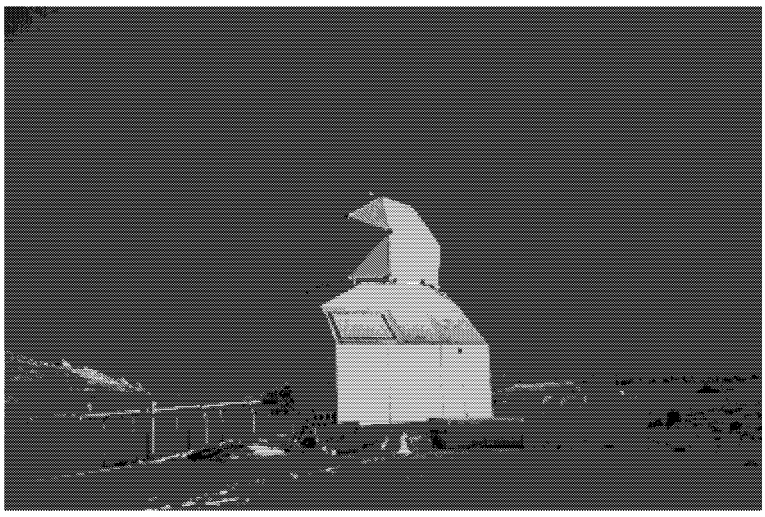

Figure 2: Photograph of the Mt. Fuji Submillimeter-wave telescope.

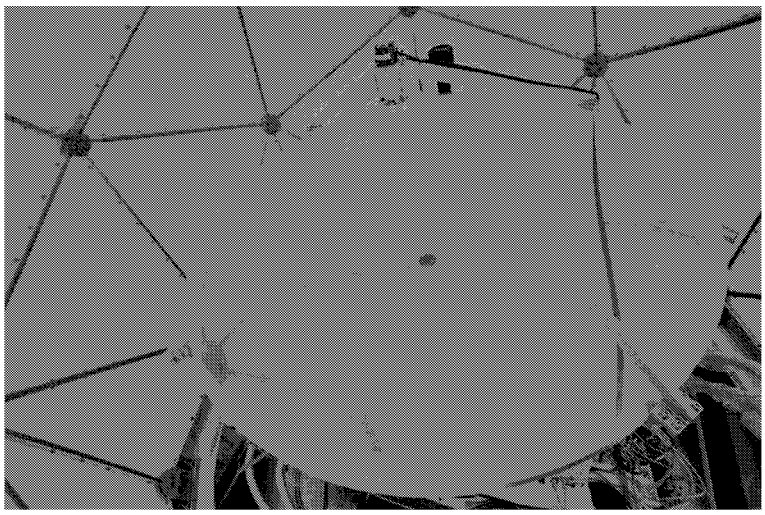

Figure 3: The main reflector of the Mt. Fuji submillimeter telescope.

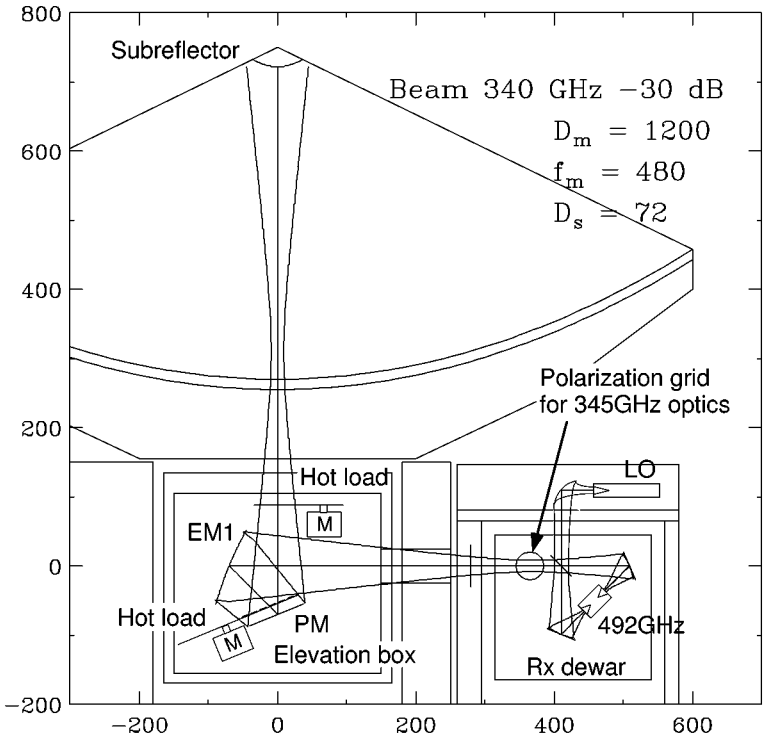

Figure 4: Optics design of the Mt. Fuji submillimeter-wave telescope. The origins of the coordinate are the azimuth axes and the elevations axes.

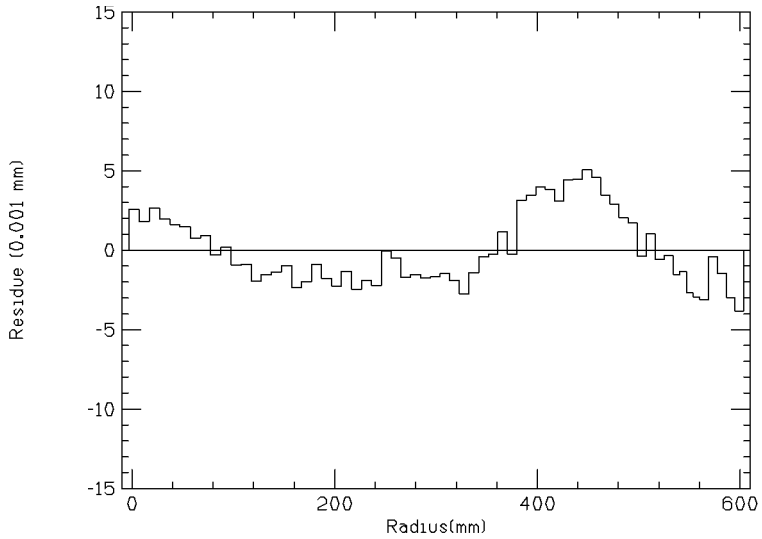

Figure 5: Residue of a parabolic template from the best fit parabola. It was used to measure a surface accuracy of the main reflector with a feeler gauge of 10μm.

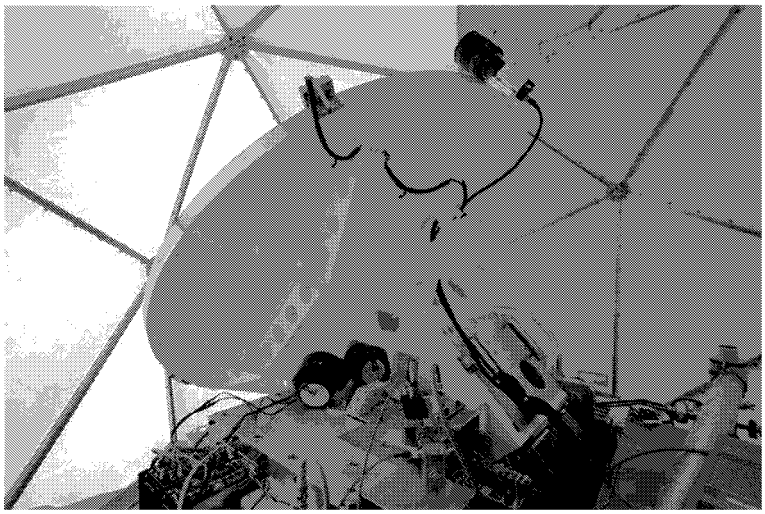

Figure 6: The backing structure of the main reflector. There is a CCD camera at the top edge of the main reflector.

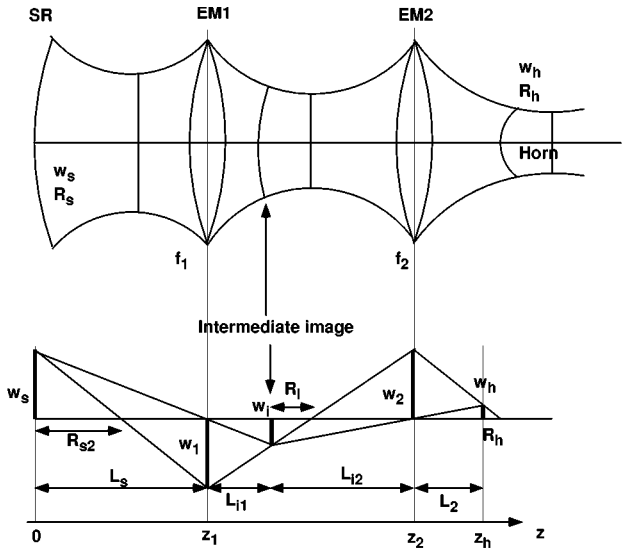

Figure 7: A definition of the optics calculation for a Gaussian beam.

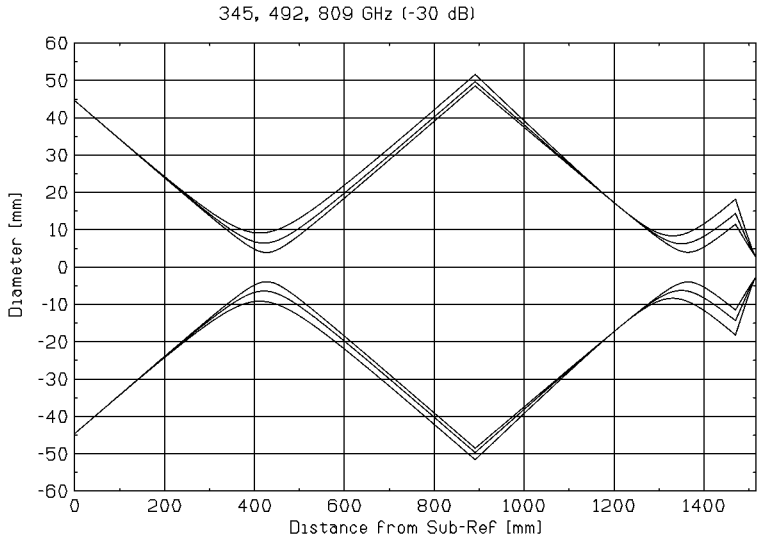

Figure 8: Beam diameter of 345, 492, and 809 GHz at an edge level of -30 dB. The inner and outer lines show a beam diameter of 809 and 345 GHz, respectively.

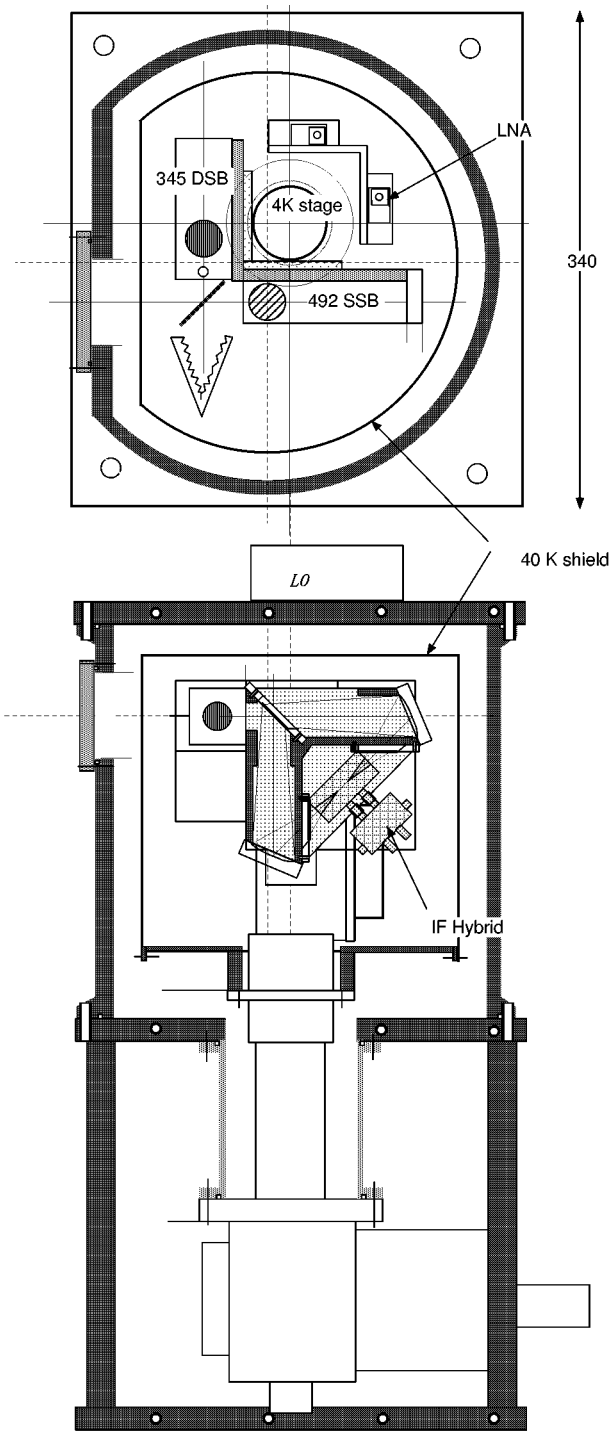

Figure 9: Schematic drawing of the receiver dewar. The dewar is made of Al.

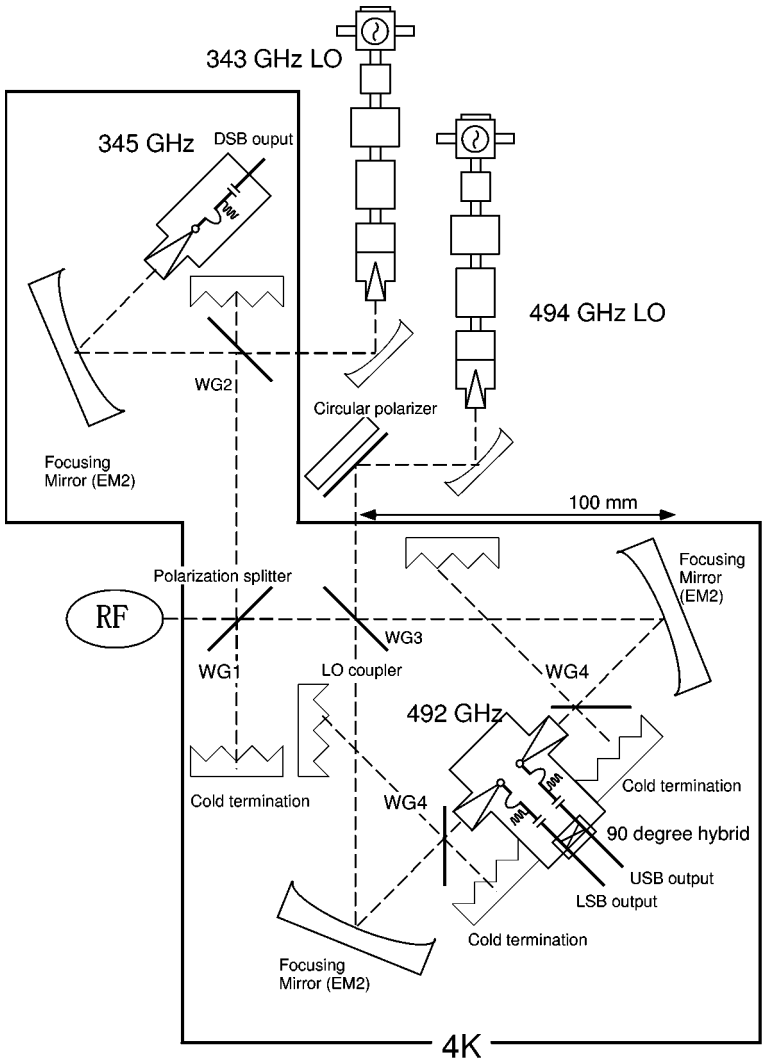

Figure 10: Schematic drawing of the 4 K optics in the dewar.

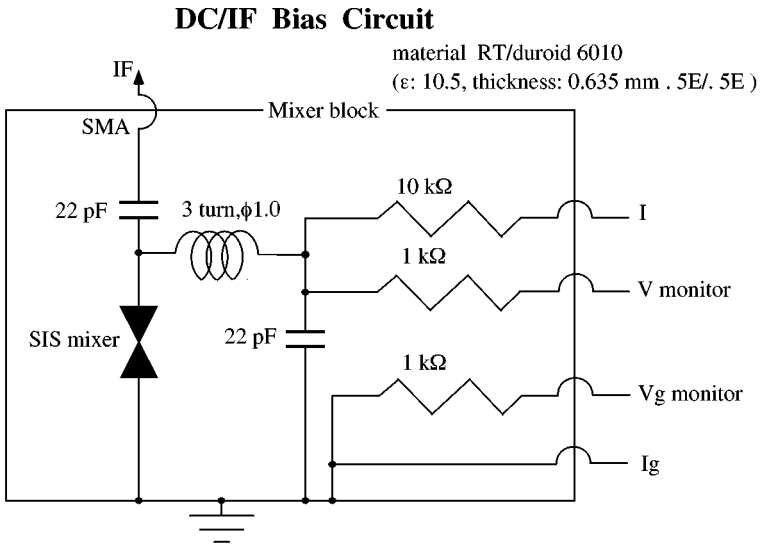

Figure 11: Schematic drawing of bias circuit for the SIS mixer

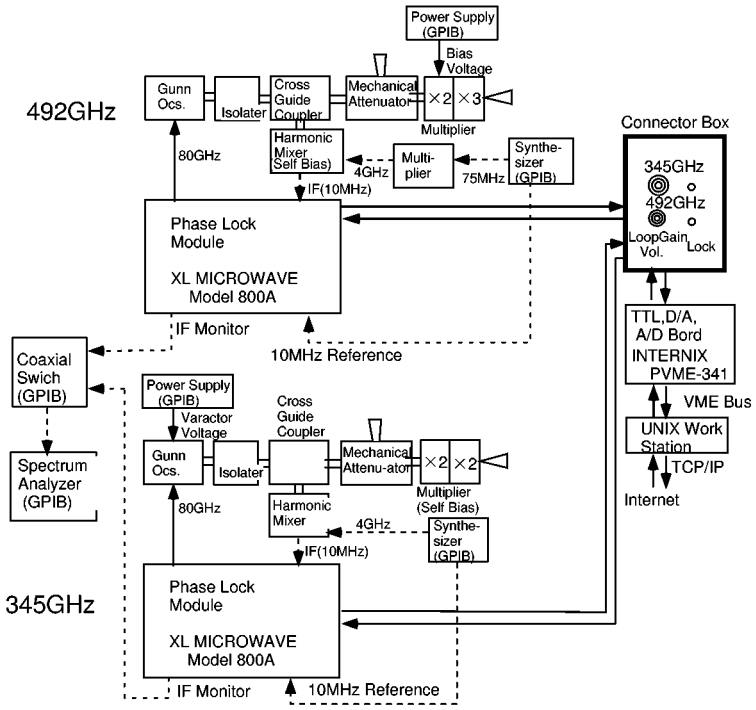

Figure 12: Schematic drawing of the local oscillators and the phase lock-loop system.

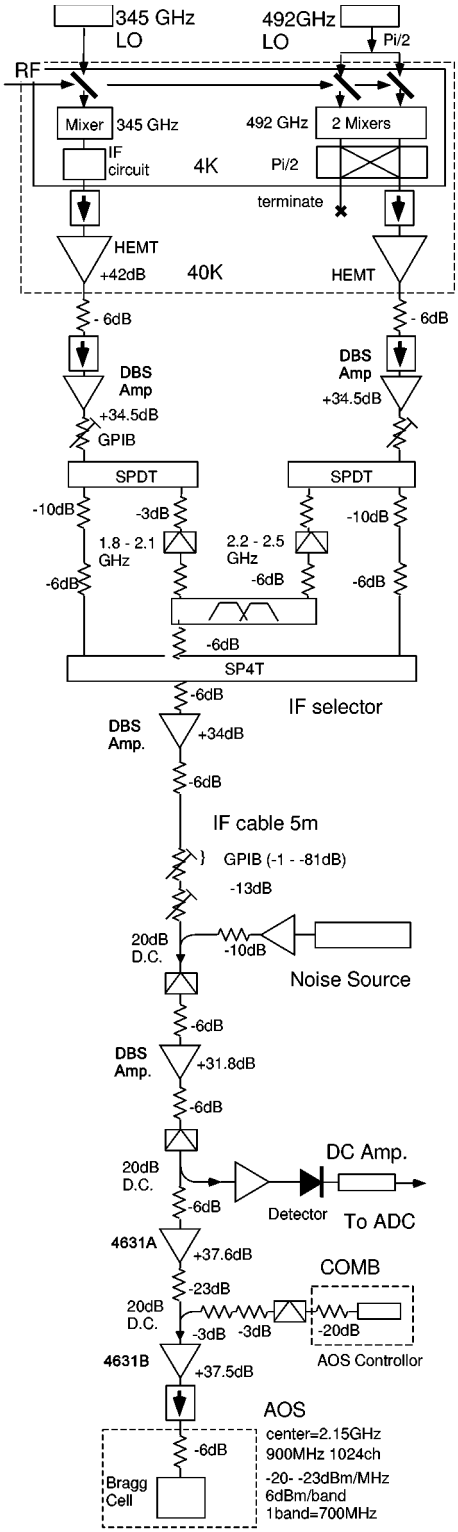

Figure 13: Schematic drawing of IF diagram

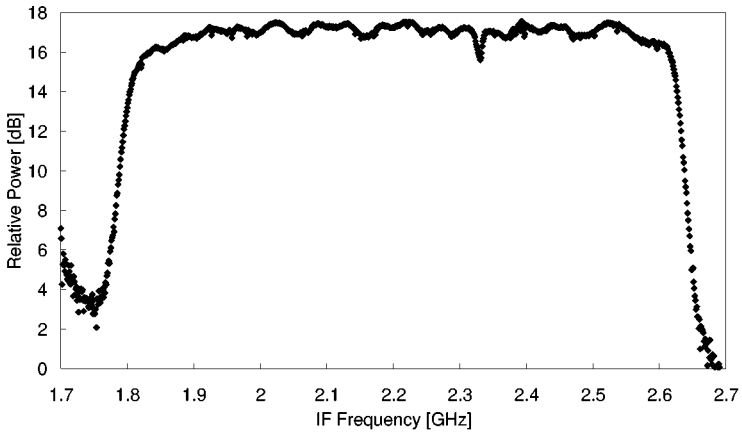

Figure 14: IF band characteristics of AOS. From 1.8 GHz to 2.6 GHz, the band flatness is less than 1 dB. The effective frequency resolution is 1.6 MHz (FWHM).

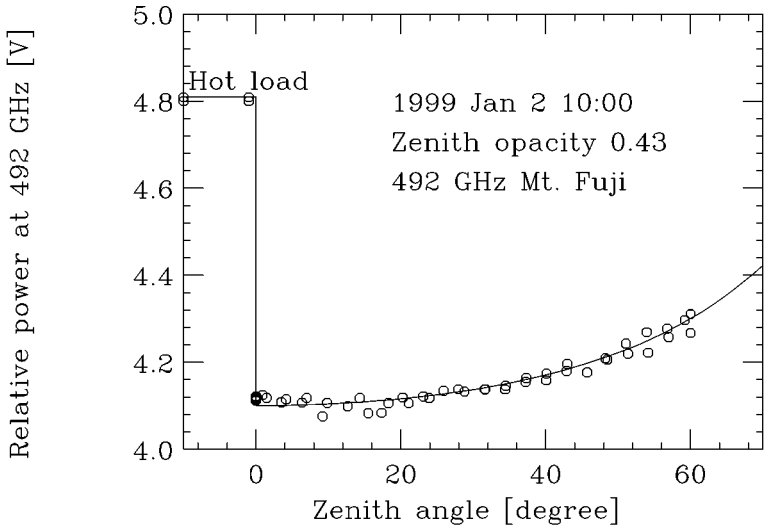

Figure 15: An example of opacity measurements obtained in Jan. 2, 1999. The data were acquired by tipping the main reflector back and forth. The solid line shows a fitted curve for hot-load temperature of 290 K and sky temperature of 253 K.

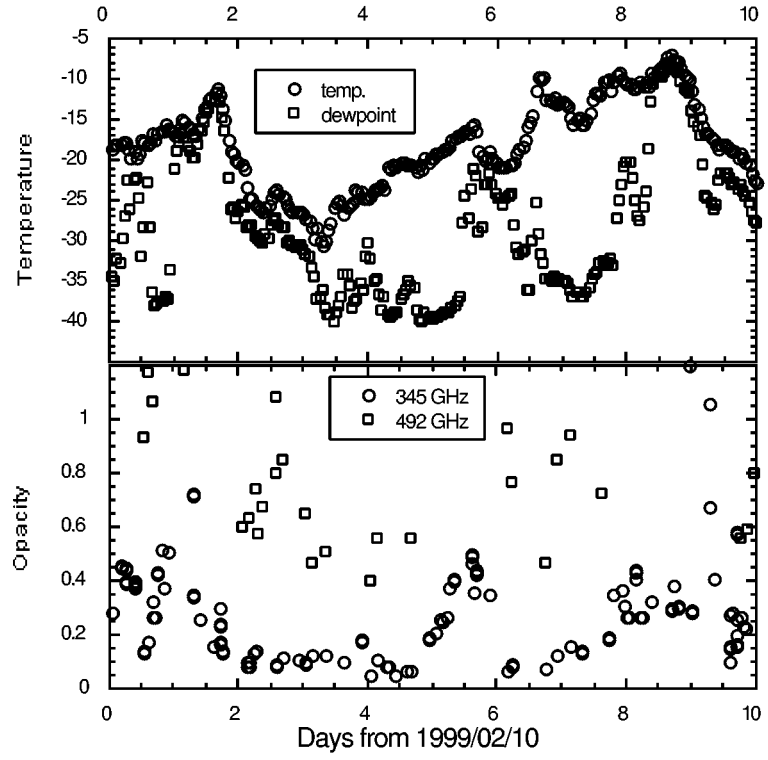

Figure 16: Atmosphric opacities at 492 GHz and 345 GHz from February 10 to February 20, 1999. Atmospheric temperature and dew point were provided by the weather station at the summit.

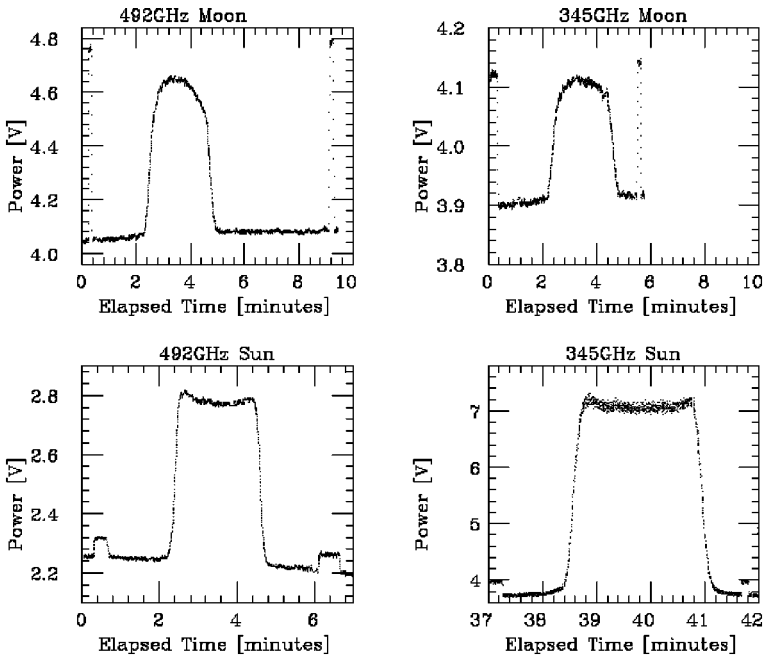

Figure 17: The moon and sun at 492 and 345 GHz. These spectra were obtained in the condition that the telescope was stopped. At the begin and end of the session, hot load calibrations were carried out.

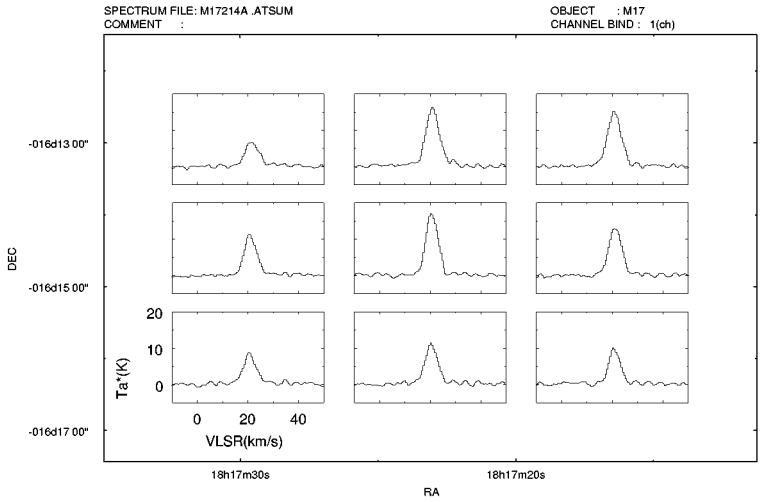

Figure 18: Example of daily intensity calibration of CI toward M17 (RA (1950) = $18^h17^m30^s$, Dec (1950) = $-16°13'0^s$) with 1.′5 grid.

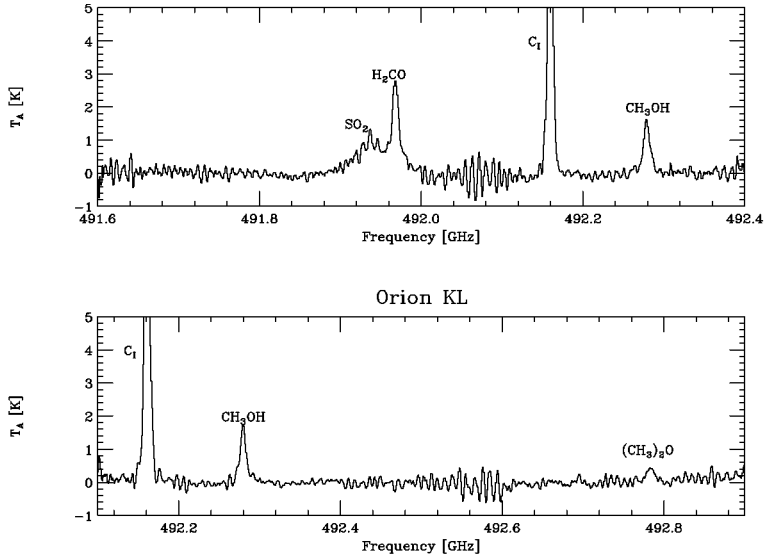

Figure 19: The 492 GHz spectra toward Orion KL

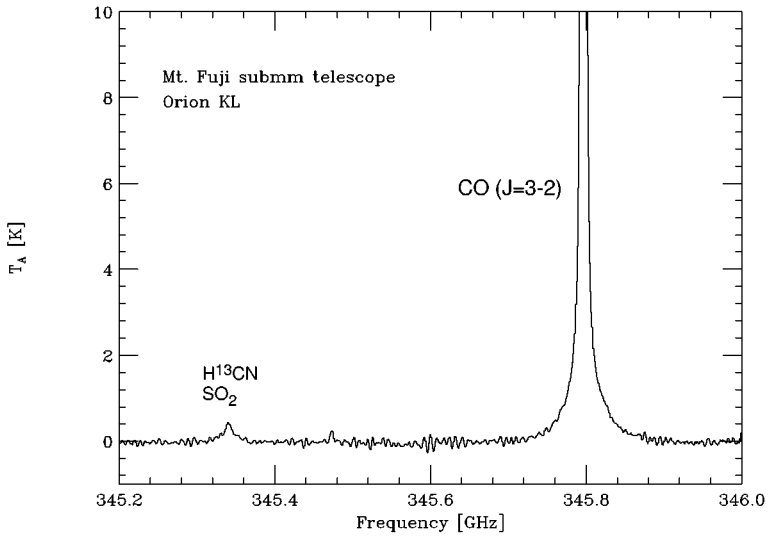

Figure 20: The 345 GHz spectra toward Orion KL obtained in the DSB receiver.

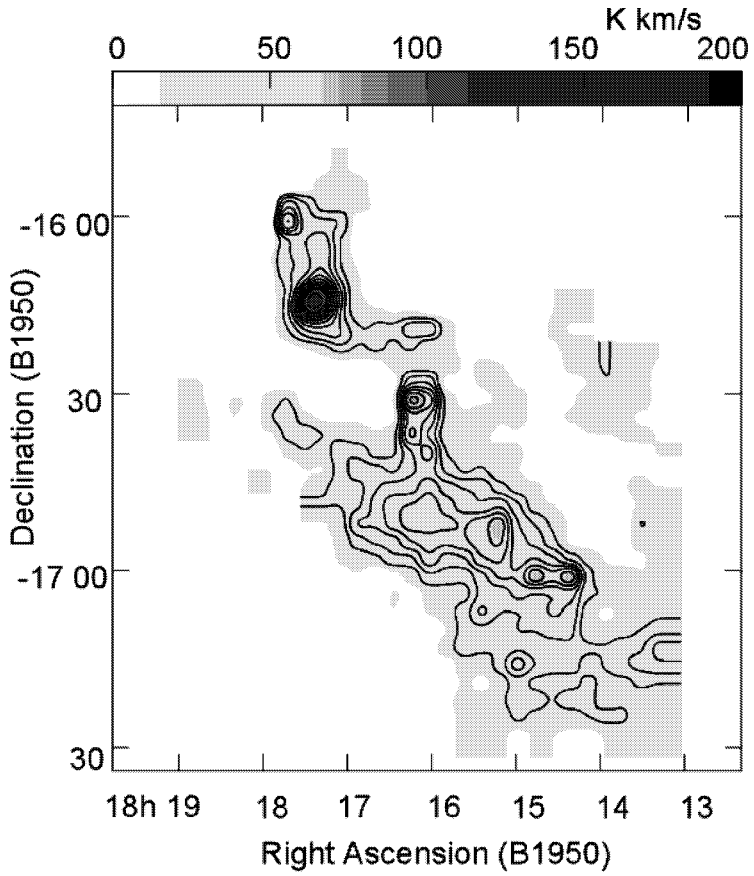

Figure 21: The integrate intensity CI map toward M17 in the velocity range from V_{lsr} = 15 km s^{-1} to 25 km s^{-1}. The lowest contour is 26 K km s^{-1}, and the step is 9 K km s^{-1}. The peak emission is 136 K km s^{-1}.

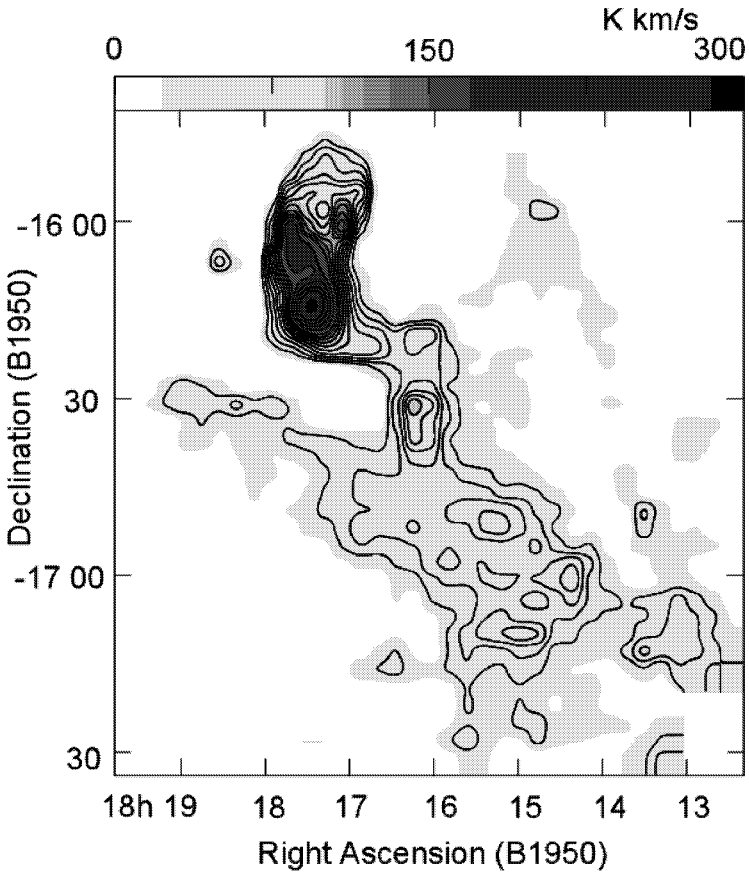

Figure 22: The integrated intensity CO ($J = 3 - 2$) map toward M17 in the velocity range from $V_{lsr} = 15$ km s^{-1} to 25 km s^{-1}. The lowest contour is 36 K km s^{-1}, and the step is 12 K km s^{-1}. The peak emission is 297 K km s^{-1}.